

Escalation of polymerization in a thermal gradient

Christof B. Mast^{a,1}, Severin Schink^{b,1}, Ulrich Gerland^b, and Dieter Braun^{a,2}

^aSystems Biophysics, Physics Department, Center for Nanoscience, and ^bArnold-Sommerfeld-Center for Theoretical Physics and Center for Nanoscience, Ludwig-Maximilians-Universität München, 80799 Munich, Germany

Edited* by Nigel Goldenfeld, University of Illinois at Urbana–Champaign, Urbana, IL, and approved April 3, 2013 (received for review March 1, 2013)

For the emergence of early life, the formation of biopolymers such as RNA is essential. However, the addition of nucleotide monomers to existing oligonucleotides requires millimolar concentrations. Even in such optimistic settings, no polymerization of RNA longer than about 20 bases could be demonstrated. How then could self-replicating ribozymes appear, for which recent experiments suggest a minimal length of 200 nt? Here, we demonstrate a mechanism to bridge this gap: the escalated polymerization of nucleotides by a spatially confined thermal gradient. The gradient accumulates monomers by thermophoresis and convection while retaining longer polymers exponentially better. Polymerization and accumulation become mutually self-enhancing and result in a hyperexponential escalation of polymer length. We describe this escalation theoretically under the conservative assumption of reversible polymerization. Taking into account the separately measured thermophoretic properties of RNA, we extrapolate the results for primordial RNA polymerization inside a temperature gradient in pores or fissures of rocks. With a dilute, nanomolar concentration of monomers the model predicts that a pore length of 5 cm and a temperature difference of 10 K suffice to polymerize 200-mers of RNA in micromolar concentrations. The probability to generate these long RNAs is raised by a factor of $>10^{600}$ compared with polymerization in a physical equilibrium. We experimentally validate the theory with the reversible polymerization of DNA blocks in a laser-driven thermal trap. The results confirm that a thermal gradient can significantly enlarge the available sequence space for the emergence of catalytically active polymers.

molecular evolution | nonequilibrium | RNA world | (nonenzymatic) emergence of RNA | hydrothermal vents

Polymers are the vital building blocks of all known life forms. According to the central dogma of molecular biology (1), DNA stores the information for how and when to build proteins, which for their part carry out catalytic tasks like the polymerization of DNA. How this self-perpetuating cycle has started is unknown. The RNA-world hypothesis posits that RNA molecules were the central players in prebiotic evolution, because they exhibit both a catalytic function similar to that of proteins and the information storage capabilities of DNA (2). However, how could such an RNA world have emerged from the prebiotic soup?

A key element of the RNA world is a ribozyme that catalyzes RNA replication. Directed in vitro evolution and engineering have shown that such ribozymes exist, but require a length of 200 bases or more, even in favorable high-salt conditions (3). Starting from chemical nonequilibrium conditions with millimolar concentrations of energy-rich nucleotides (4–6) and with the help of catalytic surfaces (7), only the formation of much shorter polynucleotides on the order of 20 bases was demonstrated in the laboratory. Slow kinetics and cleavage due to hydrolysis limit the formation of long polynucleotides and finally lead to a length distribution that decays exponentially in the case of reversible polymerization, i.e., RNA constantly being randomly built up and cleaved. A simple estimate shows that to obtain a traceable concentration of 200-mer RNAs, the concentration of nucleotides has to exceed the effective dissociation constant by at least 100-fold (Fig. S1). Plausible concentrations of nucleotides in primordial settings, e.g., a hydrothermal vent or a warm pond, should be at most in the nanomolar to low micromolar range. However, the binding affinity for nucleotide monomer binding to an oligomer is

weak, with estimates for the dissociation constant in the millimolar range (4). Even if dissociation constants in the micromolar range can be reached by specifically activated nucleotides, the non-enzymatic formation of 200-mers seems impossible in a setting that is not supported by an additional physical nonequilibrium.

In this work we demonstrate escalated polymerization in a spatially confined thermal gradient as a possible pathway for RNA to overcome this barrier. The physical nonequilibrium condition in the form of an ordinary temperature gradient will lead to exceedingly long polymers, even under the conservative assumption of reversible polymerization. In an elongated convection cell, thermophoresis accumulates macromolecules like DNA and RNA in a length-selective manner (Fig. 1A). We study how such a thermal molecule trap produces a continuing chemical nonequilibrium condition and thereby affects a weak, reversible polymerization reaction based on bonding of monomers and oligomers and random dissociation (Fig. 1B). Using a combination of experimental and theoretical methods, we identify conditions under which the interplay of these mechanisms dramatically increases the length range and efficiency of the polymerization process (Fig. 1C).

A thermal gradient in an elongated compartment arguably was an abundant physical scenario in the prebiotic world. The compartment could be a pore in volcanic rock, a cleft of mud, or a rock fissure with the temperature gradient caused by the vicinity of a warm hydrothermal or volcanic outflow into a colder ocean (8, 9). This could be found in both salty oceanic hydrothermal conditions (10) and the fresh waters near warm water ponds (11). In the laboratory, thermal molecule traps have previously been demonstrated to support accumulation of biomolecules (12, 13), formation of cell-like lipid vesicles (14), and concurrent replication and trapping with a polymerase (15, 16). Additionally, a replication of codon information using tRNA is compatible with the temperature cycling in a thermal molecule trap (17).

This previous work used the thermal trap as a passive length-selective concentration enhancer without biochemical reactions (12, 13) and replicators with fixed product length (14–16). Here, we show how the length selectivity of thermal traps and a linear polymerization reaction with arbitrary product lengths mutually enhance each other by a coupling between physical and chemical nonequilibrium (Fig. 1C): The thermal trap accumulates monomers and thereby pushes the system out of chemical equilibrium. Longer polymers are created due to the concentration-dependent polymerization. The longer polymers are accumulated more efficiently by the length-selective physical nonequilibrium of the thermal trap, which in turn leads to higher local concentrations. The positive feedback loop allows the formation of long RNA polymers even at low nucleotide concentrations. We validate our theory experimentally in the fast polymerizing regime, using a laser-

Author contributions: C.B.M., S.S., U.G., and D.B. designed research; C.B.M., S.S., U.G., and D.B. performed research; C.B.M., S.S., U.G., and D.B. analyzed data; and C.B.M., S.S., U.G., and D.B. wrote the paper.

The authors declare no conflict of interest.

*This Direct Submission article had a prearranged editor.

Freely available online through the PNAS open access option.

¹C.B.M. and S.S. contributed equally to this work.

²To whom correspondence should be addressed. E-mail: dieter.braun@lmu.de.

This article contains supporting information online at www.pnas.org/lookup/suppl/doi:10.1073/pnas.1303222110/-DCSupplemental.

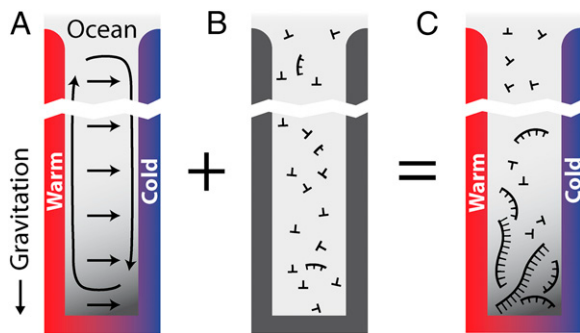


Fig. 1. Proposed polymerization in a thermal gradient: cross section of a water-filled pore that is exposed to the ocean at the top and subjected to a spatially confined horizontal temperature gradient. (A) Thermal trapping. The temperature gradient drives thermal convection (circular arrows) due to the thermal expansion of water at the hot side. Additionally, solved biomolecules move from hot to cold via thermophoresis with a drift speed $v_T = D_T \cdot \nabla T$ (horizontal arrows). In combination, solved biomolecules are accumulated at the pore bottom, exponentially dependent on their Soret coefficient $S_T \equiv D_T/D$. Because S_T increases with the molecule length, longer molecules are trapped exponentially more efficiently at the optimal trap width. (B) Polymerization. If polymerization and dissociation are in steady state, the concentration of longer polymers decays exponentially with polymer length. The mean length strongly depends on the concentration of monomers and is too short to allow for self-replicating polymers under dilute primordial conditions. (C) Trapping and polymerization. The exponential thermal accumulation can counterbalance the exponentially decaying polymerization. As a result, both the concentration and the mean length of the polymers are enhanced massively.

driven thermal trap filled with a solution of double-stranded DNA blocks, which reversibly polymerize at specifically designed sticky ends. The experiment was designed to fully control all parameters of the system. We record this polymerization process in real time and find a quantitative agreement with our theoretical model.

Theory

Thermal Molecule Trap. To study the interplay between thermal trapping and polymerization, we first describe the dynamics of each process separately and then consider the coupled processes. In a water-filled compartment, vertical gravitation and a horizontal temperature gradient ∇T lead to a laminar convective flow due to the thermal expansion of the fluid (Fig. 1A). Additionally, dissolved biomolecules with a thermodiffusion coefficient D_T will thermophoretically move along the thermal gradient with a drift speed $v_T = D_T \cdot \nabla T$. Charged molecules have a tendency to move toward the cold, a trend that can be understood from local free energy considerations (18–21). In a thermal molecule trap, both effects are combined: The biomolecules are accumulated at the bottom corner of the compartment until a steady state of thermodiffusion and the counteracting diffusion is reached. Such an accumulation effect was first observed in gases by Clusius and Dickel for chlorine isotopes (22).

We describe the accumulation of molecules inside a thermal trap, using a 2D transport equation of the drift-diffusion type for the concentration $c(x, y, t)$ of biomolecules (23),

$$\frac{\partial c}{\partial t} = D \left(\frac{\partial^2 c}{\partial x^2} + \frac{\partial^2 c}{\partial y^2} \right) + S_T D \frac{dT}{dx} \frac{\partial c}{\partial x} + v(x) \frac{\partial c}{\partial y}. \quad [1]$$

Here, x is the horizontal coordinate in Fig. 1A, y is the vertical coordinate, and t denotes time. The three terms on the right account for diffusion, thermodiffusion, and convection. The two latter effects are evoked by the linear temperature gradient $dT/dx = \Delta T/w$ over the horizontal width w of the pore, where ΔT denotes the (fixed) temperature difference between the left and right boundaries. On the one hand, the gradient yields

a thermodiffusive flux in the x direction with D the diffusion coefficient and $S_T \equiv D_T/D$ the length-dependent Soret coefficient of the dissolved molecule (18). On the other hand, thermal expansion leads to a vertical convection flow with the velocity profile $v(x)$ (SI Text A). The characteristic velocity, $v_0 = \beta g \rho \Delta T w / 72 \sqrt{3} \eta$, also depends on the gravitational acceleration g and the density ρ , viscosity η , and thermal expansivity β of the solvent (Fig. S2D).

Eq. 1 can be solved by separation of variables. In the steady state, the concentration $c(x, y) = U(x)V(y)$ increases exponentially along the vertical direction, $V(y) = \exp(-\alpha y)$ with the accumulation coefficient α fixed by the solution of $U(x)$. The detailed calculation (SI Text A) shows that $\alpha \sim S_T \partial T / \partial x$, predicting that the total accumulation in the vertical direction scales exponentially with the Soret coefficient S_T . Because longer DNA or RNA molecules have larger S_T , they can be exponentially stronger accumulated in the thermophoretic trap.

Polymerization. We describe the chemical dynamics of a generic polymerization process as a reversible aggregation–fragmentation reaction (24),

$$\frac{dc_n}{dt} = \frac{1}{2} \sum_{i+j=n} k_{ij}^{on} c_i c_j - c_n \sum_{j>0} k_{nj}^{on} c_j + \sum_{j>0} k_{nj}^{off} c_{j+n} - \frac{1}{2} c_n \sum_{i+j=n} k_{ij}^{off}, \quad [2]$$

for the concentration c_n of a polymer with length n . The concentration c_n can increase via bonding of two shorter polymers (first term on right-hand side) or via the dissociation of a longer polymer (third term), whereas it can also decrease via bonding (second term) and dissociation (fourth term). Cyclization or formation of nonproductive complexes is not considered here. The dynamics are governed by the on and off rates, k_{ij}^{on} and k_{ij}^{off} . Under the “worst-case” assumption that these rates satisfy the detailed balance condition (25) (instead of supporting a finite flux driven by a separate chemical activation process), the steady state of Eq. 2 is

$$c_n = c_1^n \prod k_{1x}^{on} / k_{1x}^{off}, \quad [3]$$

see SI Text A for details. Via summation over Eq. 3 the concentration of free monomers, c_1 can be related to the total local concentration $c_0 = \sum n c_n$ of all monomers inside a finite volume element ΔV . By inverting this functional dependence numerically, we obtain the polymer length distribution $c_n(c_0)$. The $c_n(c_0)$ fully characterizes the steady state of the polymerization process. The simplest observable is the mean polymer length $\langle n \rangle = c_0 / \sum c_n$, which corresponds to the ratio of the total monomer concentration to the total concentration of polymer molecules of any size inside ΔV . We will see that the experimental fluorescence resonance energy transfer (FRET) signal considered below is directly related to the mean length via $FRET = 1 - 1/\langle n \rangle$.

Polymerization and Trapping. The precise interplay of polymerization and thermal trapping depends on the relation between their characteristic timescales. A full analysis of the coupled dynamics would require solving Eqs. 1 and 2 simultaneously, which is computationally intensive. For our purposes it suffices to consider the two adiabatic limits of this system: The limit where the polymerization reaction is fast and always remains equilibrated during the accumulation process is adequate to describe the experiments reported below, as well as for the prebiotic scenario of RNA polymerization explored below. The opposite limit where polymerization is slow or quasi-frozen over the timescale of the accumulation is covered in SI Text C.

The characteristic timescale $\tau_a = 1/\alpha v_0$ of accumulation is the transport time for a molecule over the accumulation length scale of the trap $1/\alpha$ at the characteristic flow velocity v_0 . In the polymerization reaction, a characteristic time τ_p is obtained from the typical on rate and polymer concentration. For fast

polymerization ($\tau_p \ll \tau_a$), $c_n(c_0)$ always equilibrates according to the current local concentration $c_0 = c(x, y)$ inside the trap. One can then approximate the accumulation process by solving Eq. 1 with an effective diffusion coefficient $\bar{D}(c_0)$ and Soret coefficient $\bar{S}_T(c_0)$ (SI Text A). In the other extreme of slow polymerization ($\tau_p \gg \tau_a$), the trapped concentrations of the polymer are independently amplified for each length by the accumulation factor of the thermal trap (8).

Trapped RNA Polymerization Under Primordial Conditions. We extrapolate our theory to the scenario of RNA polymerization inside a thermal trap (8) (Fig. 2). We consider a rectangular elongated compartment and assume a reasonable temperature difference of 10 K. Smaller temperature gradients would require only linearly elongated pores with slower equilibration times (16). We assume that the pore is diffusively coupled to an infinitely large ocean or pond, and therefore we fix the local monomer concentration at the top of the pore at c_0 . The bottom of the pore is closed and the fluid flow is fully characterized by convection. We assume that the RNA polymerization reaction is in the activation-controlled regime where the diffusive association is faster than the binding reaction and the on rate is independent of length, $k_{nm}^{on} = \text{const}$. A constant off rate is a good approximation for short polymers and poses an upper bound for long polymers, because base pairing can significantly enhance the stability of a bond. As a reference, we chose an outside concentration of 1 nM and keep it smaller than the temperature-averaged dissociation constant K_D to reflect that only monomers exist in the primordial solution outside the trap.

Concerning thermophoretic properties of RNA, we use recent measurements of diffusion and Soret coefficients of RNA (20, 26) as documented in SI Text A (Fig. S3 C and D). Temperature and salt concentration play a crucial role because they have a considerable impact on the Soret coefficient of RNA. We investigated three possible primordial scenarios. For a physiological salt concentration (150 mM NaCl, $\lambda_{Debye} = 0.8$ nm) we consider an enhanced average trap temperature (55 °C, Fig. 2 and Fig. S4, III) and colder water (25 °C, Fig. S4, I). In addition, a salt-deprived scenario (3 mM NaCl, $\lambda_{Debye} = 5.6$ nm, Fig. S4, II) is analyzed, where the temperature does not change the Soret coefficients sufficiently. For the warm and salty scenario shown in Fig. 2, the experimental scaling laws for diffusion and Soret coefficients were fitted by $D(n) = 643n^{-0.46} \mu\text{m}^2/\text{s}$ and $S_T(n) = (5.3 + 5.7n^{0.73}) \times 10^{-3} \text{K}^{-1}$ (Fig. S3 C and D). Despite the fact that the Soret coefficients decrease with increasing salt concentration (18, 20), we will see that the exponential trap results in very similar outcomes for our three scenarios, demonstrating the robustness of the escalation effect.

Theoretical Results. The capability of the thermal trap to produce long polymers is shown in Fig. 2. We discuss fast polymerization (Fig. 2 A–C) and slow polymerization (Fig. S4, III) for various dissociation constants of polymerization K_D . In both regimes, polymers of considerable size are found inside the trapping region. To stay in the fast reaction regime, the relaxation time of the polymerization process has to obey $\tau_p \ll 1/\alpha v_{max} \approx 30$ min. The concentration distribution inside the compartment is solved using the adiabatic treatment described above, with effective diffusion and Soret coefficients defined according to the polymer length distribution as a function of the total concentration of monomers. Fig. 2A shows the length distribution in the chemical steady state for pore lengths between 2.5 and 4 cm (black boxes 1–4) at fixed width of 100 μm [which is optimal for the trapping of longer polymers (SI Text A)] and with a dissociation constant of $K_D = 10 \mu\text{M}$ with and without the continuing physical non-equilibrium of a thermal trap. Although dimers are barely existent outside the trap, RNA polymers of more than 100 bases are produced, exceeding even the nanomolar monomer concentration outside the trap. The dependence on trap length is illustrated in Fig. 2B. As soon as the accumulated monomer concentration reaches the threshold K_D , long polymers with higher Soret coefficients are formed. Therefore, the effective Soret coefficient \bar{S}_T becomes

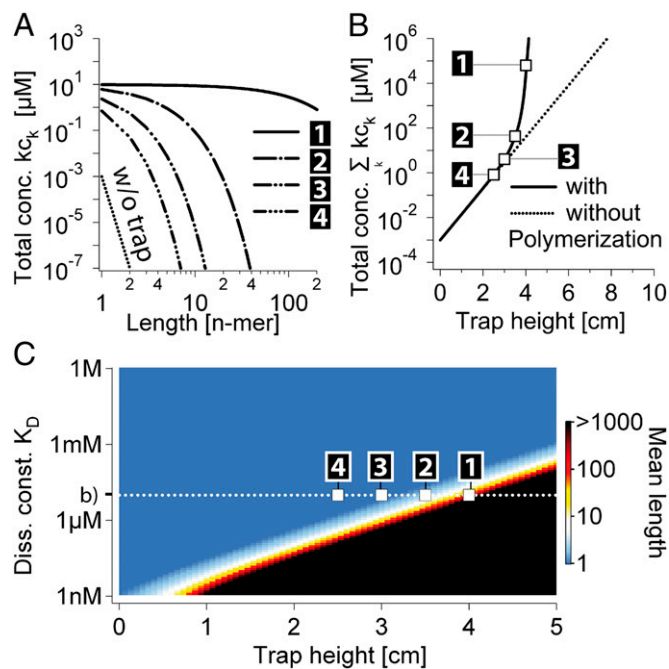


Fig. 2. RNA polymerization: accumulation and polymerization of RNA at the bottom of a primordial geothermal fissure. (A) Length distribution of a fast-reacting polymer ($\tau_p < 30$ min) inside a 2.5- to 4-cm (black boxes 1–4)-long trap at 100 μm width with a temperature difference of 10 K, an average trap temperature of 55 °C, a dissociation constant of $K_D = 10 \mu\text{M}$ for polymerization, and an outside monomer concentration of 1 nM at physiological salt concentration (150 mM NaCl, $\lambda_{Debye} = 0.8$ nm). Oligomers with the size of active ribozymes are predicted to exist in the trap. (B) Escalation of polymerization. As soon as the total concentration of RNA monomers reaches the effective Soret coefficient of the polymers increase with the trap height h_{trap} . Therefore, $c(h_{\text{trap}}) \sim \exp(\text{const} \cdot h_{\text{trap}} \cdot \bar{S}_T(h_{\text{trap}}))$ grows hyperexponentially with h_{trap} . (C) Mean polymer length vs. pore heights and a broad range of dissociation constants K_D . Even for low affinities, a plausible trap height is found at which polymerization escalates and the polymer length diverges. For polymerization slower than the accumulation, a similar behavior is found (Fig. S4, III). We conclude that the escalating growth of RNA length by a thermal trap is a robust phenomenon irrespective of the speed of polymerization.

dependent on the trap length h_{trap} , leading to a hyperexponential escalation of the total RNA concentration with the trap length according to $c(h_{\text{trap}}) \sim \exp(a \cdot h_{\text{trap}} \cdot \bar{S}_T(h_{\text{trap}}))$ with a being a constant value (Eq. S9a). The time at which hyperexponential trapping is found strongly depends on the trap length and specific shape. A 1,000-fold drop in polymerization affinity is easily balanced by a mere extension of the trap. Also a larger trap aperture presumably leads to faster trap relaxation. Because in literature values of K_D for a possible RNA polymerization reaction are only vaguely known, Fig. 2C shows the mean polymer length for a broad range of possible dissociation constants and pore lengths, including a K_D of around 10 mM for RNA polymerization measured by the Szostak group (4). In all cases, moderate trap geometries of less than 10 cm lead to polymers longer than the above-mentioned 200 nt needed for a self-replicating ribozyme. Considering the worst-case character of our reversible polymerization, models based on activated monomers are expected to generate longer polymers in even smaller traps.

For a slow polymerization ($\tau_p \gg \tau_a$), we similarly find oligomers of considerable length inside the trap (Fig. S4, III). Therefore, we conclude that the growth of RNA by a thermal trap mechanism is a robust phenomenon, significantly enhancing the range within which RNA can be polymerized, even with inefficient polymerization reactions. The escalation of polymerization by thermal traps persists over a wide range of possible primordial conditions.

Experiment

Experimental Model System. To verify the theory of accumulation-enhanced polymerization, we locally accumulated a reversibly polymerizing model system with a laser-driven thermal trap (16). The degree of polymerization as well as the local polymer concentration was measured in real time and comparable with the predicted values from theory and simulation. Care was taken to be able to define and measure all relevant parameters. In existing RNA polymerizing systems the small size of the monomers does not allow for real-time measurements in the picoliter volumes of the trap via, e.g., fluorescence microscopy. We chose larger fluorescently labeled and reversibly polymerizing DNA blocks to implement the polymerization scheme (Fig. 3A). This model system allows for a complete control over all relevant experimental parameters [D , S_T , $K_D(T)$], which is not possible in an RNA-based system to this date. Despite using DNA, the experimental realization covers all aspects of the used polymerization theory without loss of generality.

We chose two single strands of DNA with a 95-bp-long homologous sequence flanked by 25-bp long sticky ends. At experimental trap conditions, this yields a stable block of double-stranded DNA (dsDNA) with two self-complementary binding sites. The dsDNA blocks are able to reversibly bind to each other via hybridization to form polymers. The polymer-binding energies are directly correlated to the length of the sticky ends. With known hybridization kinetics of DNA, polymerization kinetics ($\tau_p \approx 10$ s) were faster than the trap kinetics ($\tau_a \approx 1$ h). To measure the degree of polymerization, each sticky end is labeled with a complementary fluorescent dye called donor and acceptor. When a dimer is created, both dyes are brought in close proximity. The donor dye is then quenched by FRET toward the acceptor dye, which will emit the transferred energy as fluorescent light. The normalized efficiency of this transfer is a direct measure for the degree of polymerization, whereas the direct acceptor

fluorescence determines the absolute concentration of dsDNA blocks. At a trap temperature of 53 °C, the initial average polymer length equilibrated at a value of 1.7 DNA blocks, which corresponds to a total average length of ~ 200 bp.

We used an improved version of the laser-driven thermal trap described in ref. 16, which allows us to set the convection speed and the temperature gradient independently of the pore width w (Fig. 3B). An infrared laser was focused inside the filled 50- μm (height) \times 100- μm (width) borosilicate capillary from below. Light absorption and the rapid movement of the IR laser along the long symmetry axis of the capillary created an elongated (length: $2 \times 3,500 \mu\text{m}$) and inwardly directed temperature gradient. Additionally, thermoviscous pumping (27) induced four symmetric convection rolls, when an asymmetric laser pattern was applied (Fig. 3C, Flow), which corresponds to four thermal traps that are connected at their hot and bottom sides as symmetric boundaries (Fig. 14 and Fig. S2). Alternating light-emitting diode (LED) excitation provided access to all four excitation and emission channels of the carboxy-X-rhodamine (ROX) and fluorescein amidite (FAM) dye, which was required to measure the fraction of closed bonds and the local concentration of monomers. A typical experimental temperature profile, monomer concentration, and FRET signal at the beginning and end of an experiment are shown in Fig. 3C.

The dsDNA block has three relevant physical parameters: The diffusion coefficient D , the Soret coefficient S_T , and the temperature-dependent monomer–monomer dissociation constant, $K_D = k_{11}^{\text{off}}/k_{11}^{\text{on}}$. We determined all three parameters in independent experiments. K_D was measured via a melting-curve analysis of a modified DNA that could form only dimers (Fig. S3A). D and S_T were both quantified by microscale thermophoresis (18, 26, 28–30), using an unreactive control monomer lacking sticky ends. To obtain the diffusion and Soret coefficients for multimers, we combined the monomer properties with the scaling laws established in ref. 18, yielding $D(n) = 65n^{-0.75} \mu\text{m}^2/\text{s}$ and $S_T(n) = 0.1n^{0.5} \text{K}^{-1}$. These experimental constraints turn Eqs. 1 and 2 into a predictive theoretical model for our system. Due to its size, the dsDNA monomer diffuses slowly and reacts quickly via base pairing; we assumed diffusion-controlled association rates between monomers and multimers, $k_{1n}^{\text{on}} \sim [D(1) + D(n)]$. As all bonds within the polymer are identical, a length-independent dissociation rate can be assumed, $k_{nm}^{\text{off}} = k^{\text{dis}}$. Taken together, this yields $k_{1n}^{\text{off}}/k_{1n}^{\text{on}} = 1.14 \times (0.5 + 0.5n^{-0.75})^{-1} \times 10^{-6} \text{M}$, which allows a theoretical prediction of the steady-state concentrations $c_n(c_0)$, using Eq. 3.

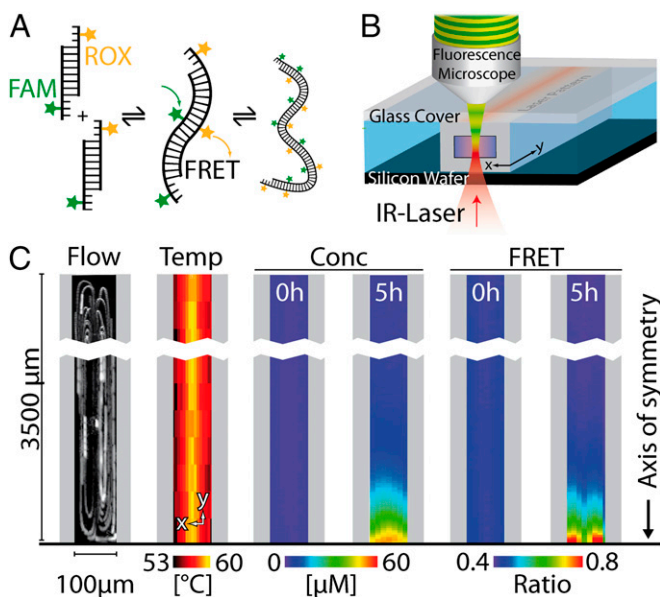


Fig. 3. Experimental model system. (A) Double-stranded DNA with two sticky ends serves as a monomer for the polymerization. The sticky ends have a melting temperature of 55 °C and are labeled with a FRET dye pair (FAM as donor, ROX as acceptor). (B) The absorption of a symmetrically moved IR laser spot in the center of a 50- μm (height) \times 100- μm (width) borosilicate capillary creates thermoviscous convection flow and thermal gradients. (C) The fluid flow has four symmetric convection rolls that model four hydrothermal pores connected at their bottom and hot sides. The temperature profile ($T = 53\text{--}60$ °C) is measured using temperature-sensitive fluorescence. The total monomer concentration c_0 is inferred from the acceptor fluorescence and the polymerization is recorded using FRET.

Experimental Results. In Fig. 4A, the time lapse of accumulation in the trap center and at the edge is shown. Laser pumping drove the fluid in circular motion at a speed of 28 $\mu\text{m}/\text{s}$ and established a temperature gradient of 7 K. Accumulation sets in immediately, depleting the edges of the trap and filling the center, reaching a constant concentration ratio between the trap center and the edge after 6 h. The edge was subsequently filled via diffusive influx from the outside of the trap, a process that is predicted to take several months (Fig. S3B). Therefore, linear syringe pumping across the capillary was performed during the complete experiment. An average flow speed of 1 $\mu\text{m}/\text{s}$ was used to enhance diffusion-driven filling of the trap in a reasonable amount of time. To describe this more complex system, we included the analytical results of Eq. 1 in a 2D finite-element simulation by considering effective diffusion and Soret coefficients \bar{D} and \bar{S}_T and a temperature-dependent dissociation constant $K_D(T)$ (Fig. S2). Because all relevant parameters [diffusion and Soret coefficients, $K_D(T)$, temperature, and convection flow velocity] were measured separately, no fit parameters were required to describe the experiment by the simulation. The 2D approximation of the 3D experimental system has been verified in previous work (8, 16). Boundary effects can be neglected for large dimensions in the z direction whereas for smaller dimensions, the effect of a parabolic profile is averaged by diffusion.

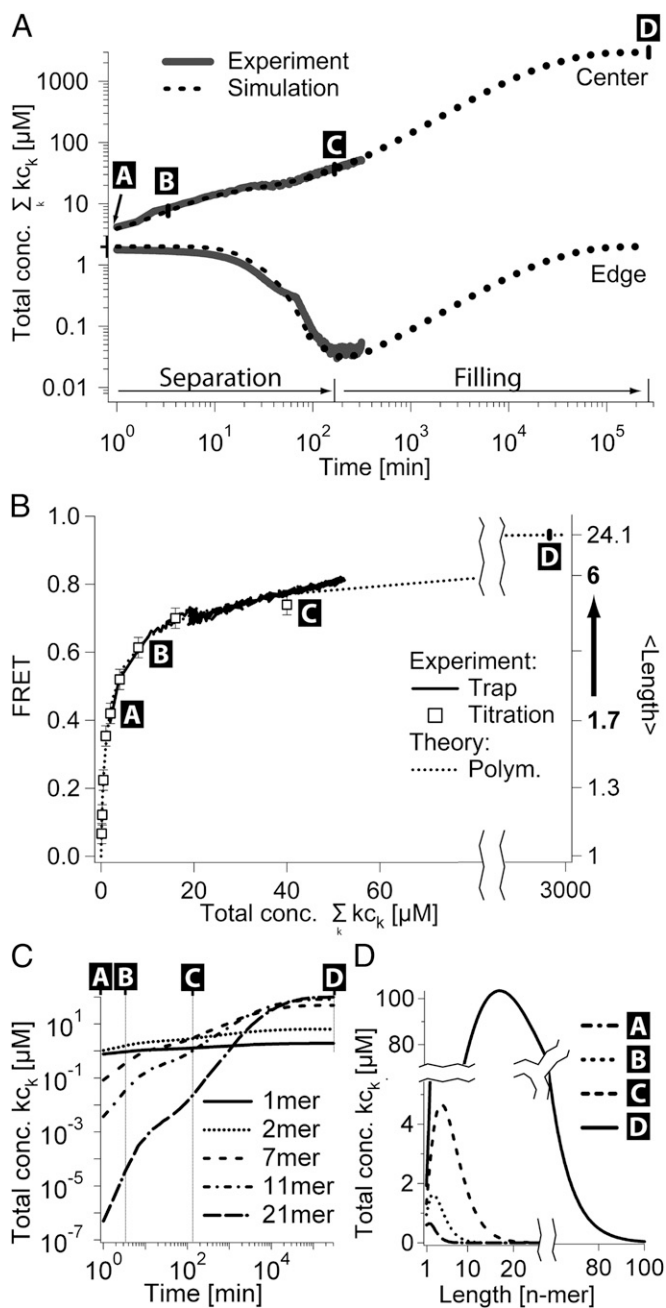


Fig. 4. Experimental data compared with simulation. (A) Simulated and measured monomer concentration in the center and at the edge of the trap with a flow-through drift of $1 \mu\text{m/s}$. The initial monomer concentration was $2 \mu\text{M}$ (time-point A). The separation ratio $\sum kc_{k,\text{center}} / \sum kc_{k,\text{edge}}$ is increased (separation phase) until the steady state of concentrations within the trap is reached after 6 h (time-point C). The monomer concentration in the trap edges is depleted by two orders of magnitude. By drift and diffusion from the surrounding bulk reservoir, the trap is filled until the trap edge reaches the concentration of the outside bulk reservoir (filling phase). Due to the restricted one-dimensional geometry outside the trap, filling is inefficient and requires several weeks (time-point D). (B) The FRET signal is a direct measure for the mean length of the polymer, plotted against the total monomer concentration in the trap center. During the complete experiment, the relationship between concentration and mean length matches the polymer theory without fitting parameters. The same relationship is obtained by titration in bulk solution (open squares). (C and D) The polymerization theory describes the time evolution of length distribution and polymer concentration. The mean polymer length increases from 1.7 (equivalent to ~ 200 bp, time-point A) to 24 monomers (equivalent to $\sim 2,880$ bp, time-point D).

Four different time points are indicated by letters A–D in Fig. 4 and Fig. S3B. After 6 h (C in Fig. 4 and Fig. S3B), the concentration ratio between the trap center and the edge reached a fixed value by reducing the monomer concentration at the trap edge. Only at a later time point (D in Fig. 4 and Fig. S3B), also the absolute monomer concentration inside the trap reached its steady state. At this time, monomers are accumulated more than 1,000-fold inside the trap. The physical nonequilibrium of the thermal trap is still required after time-point D to maintain the length-enhanced chemical equilibrium of polymerization. In Fig. 4 C and D, the polymer concentration and length distribution at the respective time points A–D of the experiment are shown. The trapped polymerization results in the concentration of 11-mers being larger than the concentration of monomers. In the final state (D in Fig. 4 and Fig. S3B), polymers consisting of 100 monomers or a corresponding length of 12,000 bp are expected. Fig. 4B shows the FRET signal recorded during the accumulation experiment (solid line). It precisely matches the theoretical prediction of our polymerization theory (dashed line), which we had calibrated using the FRET signals obtained by titration in a heated, non-convecting, nonaccumulating trap (open squares).

Assumptions, such as the omission of cyclization reactions and the diffusion-controlled limit for the experimental system, are supported by the agreement of Eq. 2 to the titration values. Furthermore, the agreement between the dynamic and static experiments (Fig. 4B) shows that at every time point polymerization is faster than the thermal trap as assumed in theory. This corresponds to a small perturbation of the chemical equilibrium of polymerization by the continuing physical nonequilibrium of the thermal trap until the final length distribution is reached. This gives us the confidence to extrapolate the findings toward a prebiotic scenario, implemented solely by using the experimentally verified theory of accumulation-enhanced polymerization, but with RNA parameters and a gravitationally driven trap instead of a laser-driven one.

Discussion

Our detailed theory to describe accumulation and polymerization in a thermal gradient is based on realistic assumptions and uses experimentally measured parameters. It connects physical and chemical nonequilibrium systems that are plausible in a primordial setting. The polymerization of RNA in thermal traps can be predicted because reliable measurements of the thermophoretic parameters of RNA for different lengths at various salt concentrations are available. In various scenarios, a critical length of the trap is found for which the accumulation reaches the dissociation constant of polymerization. Beyond this critical trap length, the trapped concentration diverges hyperexponentially and the RNA length distribution reaches lengths beyond 100 bases (Fig. 2C). Because the thermophoretic coefficients depend only moderately on concentration, significant reductions of the ionic contributions to thermophoresis are expected only well beyond millimolar concentrations (18) and are unlikely to vanish due to hydrophobic contributions.

The kinetics of the trap can require weeks and years in the simple linear geometry discussed here. As the outside molecules have to access the trap by diffusion, the equilibration timescale of the trap increases linearly with the concentration ratios. Reaching the point (2) in Fig. 2A–C by pure linear diffusion demands 100 y. However, alternative geometries with, e.g., a larger trap aperture for increased diffusive influx or with a continuous overflow of ocean water perpendicular to the hydrothermal convection allow reaching the steady state much faster.

The proposed mechanism of trapped polymerization is well suited for low salt concentrations used, for example, in RNA polymerization from cyclic nucleotides (5). The polymerization requires cGMP in millimolar concentrations, which could be enriched from catalytically active rock surfaces (31). In general, surface catalysis on rock particles of the micrometer scale such as clay (7) is highly compatible, because larger particles show only minor accumulation due to their slow diffusional response time. For example, 1- μm beads cycle under conditions at which DNA

strongly accumulates (Movie S1), forcing molecules to reversibly attach and detach at the particle surface.

The thermal gradient and convection not only support accumulation and polymerization but also are capable of triggering and preserving the propagation of information, a vital requirement of the RNA world. When following a convection path, oligonucleotides are exposed to temperature oscillations that can trigger exponential replication reactions (15, 16). Compared with the isothermal case, replication is not faster for shorter oligomers and thus does not lead to the degeneration of information by shortening of the replicates as demonstrated by Spiegelmann's pioneering experiments (32). Thermally triggered replication (PCR) is compatible with thermal trapping: In previous work, DNA was replicated with a polymerase every 30 s in a laser-driven thermal molecule trap (16). Also the protein-free replication of codon information can be approached by using truncated tRNA molecules in a thermal oscillation (17). Other physical nonequilibrium mechanisms to drive replication have also been explored, such as a mechanical disequilibrium-induced pattern of replication in larger DNA complexes (33). Isothermal RNA ligation could be used for a mutual ligation chain reaction (34). Techniques from DNA machines could be used to form oligomers (35) and trigger sequence-determined polymer synthesis (36). Interestingly, important steps in peptide synthesis can be catalyzed by simple RNA molecules under physiological conditions (37). In addition, it was recently shown theoretically by modeling RNA ligation in a thermophoretic trap that sequence information transmission can be initiated by differential degradation in a thermal oscillation (38). More generally, the framework of nonequilibrium statistical thermodynamics can be used as a unifying theoretical framework to describe the generation of sequence information, using chemical and physical nonequilibrium processes (39). An exciting experimental prospect is the implementation of autonomous

molecular evolution in a thermal trap—a molecular Darwinian process with replication driven by thermal cycling and selection driven by the length-sensitive trapping.

Materials and Methods

The trapping geometry and laser heating were described previously (16). Trap length was increased to 3.5 mm on each side (aspect ratio of the trap 70 from each side) at a lower temperature difference by plan correcting the scanning optics (specifications provided in *SI Text B*). A capillary with a rectangular cross section of $100 \times 50 \mu\text{m}$ was thermally coupled to a Peltier element with sapphire and silicon. Double-stranded DNA with a length of 95 bp and with sticky ends 25 bases in length was allowed to reversibly polymerize by hybridization. Physiological salt concentrations ($1 \times \text{PBS}$: 137 mM NaCl, 2.7 mM KCl, 10 mM $\text{Na}_2\text{HPO}_4 \cdot \text{H}_2\text{O}$, 2 mM KH_2PO_4 , pH 7.4) were used throughout the experiment. Heating and thermoviscous flow were provided by a 1,940-nm IR laser (20 W; IPG Photonics) and calibrated with the temperature-dependent fluorescence of the FRET signal and silica beads, respectively. DNA binding was recorded with fluorescence energy transfer (Table S1 and S2) (40) in an alternative dual excitation and permanent dual emission (Optosplit II; Cairn Research) microscopy setup (Axiovert Vario; Zeiss) with a 40 \times , 0.9 NA objective (Zeiss). Multiple images at modulated LED currents were used to enhance the dynamic range of the 12-bit CCD camera (PCO imaging). The thermophoretic properties (diffusion and Soret coefficient) of the 95-bp DNA were measured as described previously (20). To extrapolate the experiments into an RNA-world scenario, short single-stranded RNAs with lengths of 5–50 bases were measured over various salt concentrations and temperatures (*SI Text C*). Soret coefficients vs. RNA over length were fitted with power laws for use in theory and finite-element simulations.

ACKNOWLEDGMENTS. We thank Mario Herzog for measuring the thermophoretic properties of short nucleotides. Michael Nash, David Smith, Moritz Kreising, and Ernesto di Mauro gave valuable comments on the manuscript at various stages. We thank Ingo Stein and Philip Tinnfeld in the analysis of FRET efficiencies. Financial support from the NanoSystems Initiative Munich, the Ludwig-Maximilians-Universität Munich Initiative Functional Nanosystems, the International Doctorate Program NanoBioTechnology, and the European Research Council Starting Grant is acknowledged.

- Crick F (1970) Central dogma of molecular biology. *Nature* 227(5258):561–563.
- Gilbert W (1986) Origin of life: The RNA world. *Nature* 319:618.
- Wochner A, Attwater J, Coulson A, Holliger P (2011) Ribozyme-catalyzed transcription of an active ribozyme. *Science* 332(6026):209–212.
- Zhang N, Zhang S, Szostak JW (2012) Activated ribonucleotides undergo a sugar pucker switch upon binding to a single-stranded RNA template. *J Am Chem Soc* 134(8):3691–3694.
- Costanzo G, Pino S, Ciciriello F, Di Mauro E (2009) Generation of long RNA chains in water. *J Biol Chem* 284(48):33206–33216.
- Costanzo G, et al. (2012) Generation of RNA molecules by a base-catalyzed click-like reaction. *ChemBioChem* 13(7):999–1008.
- Ferris JP, Hill AR, Jr., Liu R, Orgel LE (1996) Synthesis of long prebiotic oligomers on mineral surfaces. *Nature* 381(6577):59–61.
- Baaske P, et al. (2007) Extreme accumulation of nucleotides in simulated hydrothermal pore systems. *Proc Natl Acad Sci USA* 104(22):9346–9351.
- Mielke RE, et al. (2011) Iron-sulfide-bearing chimneys as potential catalytic energy traps at life's emergence. *Astrobiology* 11(10):933–950.
- Martin W, Baross J, Kelley D, Russell MJ (2008) Hydrothermal vents and the origin of life. *Nat Rev Microbiol* 6(11):805–814.
- Morgan L, et al. (2003) Exploration and discovery in Yellowstone Lake: Results from high-resolution sonar imaging, seismic reflection profiling, and submersible studies. *J Volcanol Geotherm Res* 122:221–242.
- Weinert FM, Braun D (2009) An optical conveyor for molecules. *Nano Lett* 9(12):4264–4267.
- Braun D, Libchaber A (2002) Trapping of DNA by thermophoretic depletion and convection. *Phys Rev Lett* 89(18):188103.
- Budin I, Bruckner RJ, Szostak JW (2009) Formation of protocell-like vesicles in a thermal diffusion column. *J Am Chem Soc* 131(28):9628–9629.
- Braun D, Goddard NL, Libchaber A (2003) Exponential DNA replication by laminar convection. *Phys Rev Lett* 91(15):158103.
- Mast CB, Braun D (2010) Thermal trap for DNA replication. *Phys Rev Lett* 104(18):188102.
- Krammer H, Möller FM, Braun D (2012) Thermal, autonomous replicator made from transfer RNA. *Phys Rev Lett* 108(23):238104.
- Duhr S, Braun D (2006) Why molecules move along a temperature gradient. *Proc Natl Acad Sci USA* 103(52):19678–19682.
- Dhont JKG, Wiegand S, Duhr S, Braun D (2007) Thermodiffusion of charged colloids: Single-particle diffusion. *Langmuir* 23(4):1674–1683.
- Reineck P, Wienken CJ, Braun D (2010) Thermophoresis of single stranded DNA. *Electrophoresis* 31(2):279–286.
- Ludwig C (1856) Diffusion zwischen ungleich erwärmten Orten gleich zusammengesetzter Lösungen [Diffusion of homogeneous fluids between regions of different temperature]. *Sitzungsbericht Kaiser Akad Wiss*, ed Braunmüller W (Mathem-Naturwiss Cl, Vienna), Vol 65, p 539. German.
- Clusius K, Dickel G (1938) Neues verfahren zur gasentmischung und isotopentrennung [A new method for the separation of different gases and isotopes]. *Naturwissenschaften* 26:546. German.
- Debye P (1939) Zur theorie des clusius'schen trennungsverfahrens [Theory about the Clusius separation process]. *Ann Phys* 428:284–294. German.
- Krapivsky PL, Redner S, Ben-Naim E (2010) *A Kinetic View of Statistical Physics* (Cambridge Univ Press, Cambridge, UK).
- van Kampen NG (1992) *Stochastic Processes in Physics and Chemistry* (North-Holland Personal Library, Amsterdam).
- Wang Z, Kriegs H, Wiegand S (2012) Thermal diffusion of nucleotides. *J Phys Chem B* 116(25):7463–7469.
- Weinert FM, Braun D (2008) Optically driven fluid flow along arbitrary microscale patterns using thermoviscous expansion. *J Appl Phys* 104:104701–104701-10.
- Duhr S, Braun D (2006) Optothermal molecule trapping by opposing fluid flow with thermophoretic drift. *Phys Rev Lett* 97(3):038103.
- Seidel SAI, et al. (2012) Label-free microscale thermophoresis discriminates sites and affinity of protein-ligand binding. *Angew Chem Int Ed Engl* 51(42):10656–10659.
- Wang X, et al. (2011) Peptide surfactants for cell-free production of functional G protein-coupled receptors. *Proc Natl Acad Sci USA* 108(22):9049–9054.
- Saladino R, Botta G, Pino S, Costanzo G, Di Mauro E (2012) Genetics first or metabolism first? The formamide clue. *Chem Soc Rev* 41(16):5526–5565.
- Spiegelmann F, Haruna I, Holland IB, Beaudreau G, Mills D (1965) The synthesis of a self-propagating and infectious nucleic acid with a purified enzyme. *Proc Natl Acad Sci USA* 54(3):919–927.
- Schulman R, Yurke B, Winfree E (2012) Robust self-replication of combinatorial information via crystal growth and scission. *Proc Natl Acad Sci USA* 109(17):6405–6410.
- Lincoln TA, Joyce GF (2009) Self-sustained replication of an RNA enzyme. *Science* 323(5918):1229–1232.
- Lubrich D, Green SJ, Turberfield AJ (2009) Kinetically controlled self-assembly of DNA oligomers. *J Am Chem Soc* 131(7):2422–2423.
- McKee ML, et al. (2010) Multistep DNA-templated reactions for the synthesis of functional sequence controlled oligomers. *Angew Chem Int Ed Engl* 49(43):7948–7951.
- Turk RM, Chumachenko NV, Yarus M (2010) Multiple translational products from a five-nucleotide ribozyme. *Proc Natl Acad Sci USA* 107(10):4585–4589.
- Obermayer B, Krammer H, Braun D, Gerland U (2011) Emergence of information transmission in a prebiotic RNA reactor. *Phys Rev Lett* 107(1):018101.
- Andrieux D, Gaspard P (2008) Nonequilibrium generation of information in copolymerization processes. *Proc Natl Acad Sci USA* 105(28):9516–9521.
- Förster T (1948) Zwischenmolekulare Energiewanderung und Fluoreszenz [Inter-molecular energy transfer and fluorescence]. *Ann Phys* 437:55–75. German.

Supporting Information

Mast et al. 10.1073/pnas.1303222110

SI Text A. Theory

Equilibrium Solution of the Polymer Length Distribution. In this section, we describe the derivation and limitations of the solution of the aggregation–fragmentation model outlined in the main text. The aggregation–fragmentation type Eq. 2 rewritten more compactly as

$$\frac{dc_n}{dt} = \frac{1}{2} \sum_{ij} [k_{ij}^{\text{on}} c_i c_j - k_{ij}^{\text{off}} c_{i+j}] [\delta_{i+j,n} - \delta_{i,n} - \delta_{j,n}] \quad \text{[S1]}$$

(using the Kronecker-Delta, $\delta_{i,j} = 0$ for $i \neq j$ whereas $\delta_{i,i} = 1$) has a very simple stationary solution if there is a set of concentration values c_i that makes the first bracket in the sum vanish for every i, j . This condition is equivalent to the condition of detailed balance, i.e., the balance of all fluxes with their respective counterfluxes, $k_{ij}^{\text{on}} c_i c_j = k_{ij}^{\text{off}} c_{i+j} \forall i, j$. Such a set of concentration values c_i does not always exist, i.e., not for any set of rates k_{ij}^{on} and k_{ij}^{off} , but only if these rate constants satisfy certain constraints (one way to formulate and check these constraints is the Kolmogorov criterion, which demands that for every loop in state space, the product of all forward rates must be equal to the product of all backward rates). A physical system whose dynamics are described by a set of rate constants with this property is said to obey detailed balance. Detailed balance is guaranteed for a closed system that has reached full equilibrium, but not for nonequilibrium systems such as the thermal trap. However, for our description of the experiment in the main text, we assume an adiabatic accumulation limit where the thermal disequilibrium generated by the external temperature gradient does not destroy detailed balance in the chemical reactions. In this limit, the nonequilibrium steady state of the (reversible) polymerization process in the thermal trap corresponds to the equilibrium state of the same chemical process at an elevated total monomer concentration. This assumption is physically plausible and justified a posteriori by our finding that it yields an accurate description of the experiment.

To determine a set of rate constants k_{ij}^{on} and k_{ij}^{off} that is consistent with our independent measurements (diffusion constants and monomer–monomer binding equilibrium) and also obeys detailed balance, we posit that each bond breaks with equal probability and thus all dissociation rates are equal, $k_{ij}^{\text{off}} = \text{const}$. Because we are ultimately interested only in the steady-state concentrations, c_n , the numerical value of this constant does not affect the final result (it cancels out) and need not be specified. The measured monomer–monomer dissociation constant, $K_D = k_{11}^{\text{off}}/k_{11}^{\text{on}} = 1.14 \times 10^{-6}$ M, then fixes the monomer–monomer association rate. Assuming that the association is diffusion limited, our experimentally determined scaling of the diffusion coefficient with oligomer length, $D(n) = 643n^{-0.46} \mu\text{m}^2/\text{s}$, can be used to extrapolate the monomer–monomer association rate to reactions with longer molecules. Specifically, we use this scaling to estimate the rates for monomer binding to a multimer according to $k_{1n}^{\text{on}} \propto [D(1) + D(n)]$, because the diffusion coefficient of the relative coordinate is the sum of the diffusion coefficients of the two molecules in a binary reaction. All remaining rates are then fixed by the detailed balance condition, because every multimerization state can be reached by consecutively adding monomers, and detailed balance requires that the product of equilibrium constants be the same along all pathways to a given multimerization state. The concentration of n -mers is then simply related to the free monomer concentration c_1 by $c_n = c_1^n \prod_{ij} k_{ij}^{\text{on}}/k_{ij}^{\text{off}}$.

For our extrapolation of the prebiotic scenario for RNA polymerization, we use the same framework, but assume activation-

controlled bond formation, with an association rate that is independent of the molecule lengths, $k_{nm}^{\text{on}} = \text{const}$. Taking the dissociation rate to be constant as well (as before), the distribution of polymer lengths becomes exponential, $c_n = c_1^n (k^{\text{on}}/k^{\text{off}})^{n-1}$. This choice of rates automatically fulfills detailed balance. As detailed below, we chose K_D to be averaged over temperature and temperature independent, because it deviates less than one order of magnitude within the considered temperatures perpendicular to the trap (Eq. S13) and the temperature does not vary along the trap.

Estimating the Concentration of Long Polynucleotides in Equilibrium.

Although the detailed chemical pathway under which polynucleotides could have been formed from individual building blocks is still under debate, one can point out the regime in which long polynucleotides are expected. Although covalent bonds formed between nucleotides are relatively stable, the possibility for cleavage due to hydrolysis increases with each newly added nucleotide. The competition between formation and cleavage leads to an equilibrium distribution of finite polynucleotide lengths. Assuming random association and dissociation, we use the aggregation–fragmentation Eq. 2. For an activation-controlled reaction, see the discussion following Eq. 2, where the concentration of polynucleotides decays exponentially with length $c_n = c_1 (c_1/K_D)^{n-1}$. The total concentration of nucleotides $c_0 = \sum n c_n$ can be expressed in terms of monomer concentration c_1 and dissociation constant K_D . The functional dependence can be inverted analytically to

$$c_1(c_0, K_D) = 1 + \frac{K_D}{2c_0} - \frac{\sqrt{(K_D(K_D + 4c_0))}}{2c_0} \quad \text{[S2]}$$

The concentration distribution c_n as a function of the polymerization strength c_0/K_D is shown in Fig. S1. For concentrations lower than the dissociation constant, almost only monomers exist in equilibrium. Long polynucleotides are virtually nonexistent in this regime. For instance, 200-mers are expected to appear as little as $\sim c_0 \times 10^{-600}$. Long polynucleotides appear abruptly as soon as the concentration exceeds the dissociation constant by orders of magnitude.

Derivation of Accumulation Formulas. a) Gravitationally driven trap.

Debye's approach for the thermophoretic trap was used to derive an analytic result for the accumulation distribution inside the trap. This derivation is now laid out in detail for both laser and gravitationally induced pumping. As explained in the main text, the pore is modeled by an elongated 2D compartment orientated in a vertical y direction. A temperature gradient is applied in a horizontal x direction, by keeping the two walls facing each other at a constant temperature, one being warm and the other one cold. The 2D approximation of the simulation and theory was shown to successfully describe the 3D experiment and theoretical treatments in previous work (1, 2). This is reasonable because flow velocities in the z direction are much smaller than the convection flow along the y axis induced by gravitation or, in the experiment, by a moving laser spot. For thermophoresis, only the component along the thermal gradient (here, along the x axis) to the convection flow will contribute to the strong accumulation of the thermal trap. Minor thermal gradients, created by the glass surfaces of the capillary, give a much smaller thermophoretic movement along the z and y axes, both contributions that can be neglected. Likewise, diffusion was

shown to average well over existing parabolic flow profiles in three dimensions. As discussed and treated in ref. 1, a variety of chambers with different z dimensions showed equal accumulation strengths. Thus, to describe the experiment, it is sufficient to consider the measured experimental data (temperature, fluid flow profile) only in two dimensions. Please note that all measurements are averaged along the z axis by the epifluorescent measurement. The drift-diffusion equation

$$\frac{\partial c}{\partial t} = D \left(\frac{\partial^2 c}{\partial x^2} + \frac{\partial^2 c}{\partial y^2} \right) + S_T D \frac{dT}{dx} \frac{\partial c}{\partial x} + v(x) \frac{\partial c}{\partial y} \quad [\text{S3}]$$

is steered by three contributions: diffusion, thermodiffusion, and convection. Sedimentation of DNA or RNA is not considered here, because even for large T4-DNA with a length of 169 kbp and a sedimentation coefficient $s \sim 100$ S, the sedimentation speed $v_{sed} = g \cdot s = 0.1$ nm/s at gravitational acceleration g is $>10,000$ -fold slower than convection and can be neglected (3, 4). The following two effects are directly evoked by a linear temperature gradient $dT/dx = \Delta T/w$ over the width w of the compartment. On the one hand the gradient yields a thermodiffusive flux in the x direction with D and S_T being the diffusion and Soret coefficient of the dissolved molecule. On the other hand, particles are transported via convection. The driving effect for convection in a horizontally erected, elongated pore is the expansivity β of the solvent. Difference in density yields differences in gravitational force per volume. Debye derived from the equilibrium of forces for a volume element a dependence of the velocity in the y direction on the x position:

$$\frac{\partial^3 v}{\partial x^3} = \frac{-\beta g \rho \Delta T}{\eta w}. \quad [\text{S4}]$$

This factor depends on the natural constants solvent density ρ , viscosity η , and thermal expansivity β , as well as width w and temperature difference ΔT , and holds as long as temperature-induced changes in expansivity can be neglected. Far from the ends of the trap, the flow is solely directed in the y direction, thus meaning that the velocity profile in the x direction is independent of y . In this case, the velocity profile can be solved via integration. With no slip boundaries at both walls, $v(0) = 0$, $v(w) = 0$. As a side condition, because no drift through the pore is assumed, the total flow up and down must cancel for the system to conserve mass. This yields the velocity profile (Fig. S2D)

$$v(x) = \frac{-\beta g \rho \Delta T w}{6\eta} \left(\frac{1}{2} \frac{x}{w} - \frac{3}{2} \frac{x^2}{w^2} + \frac{x^3}{w^3} \right) = -v_0 \left(\frac{1}{2} \frac{x}{w} - \frac{3}{2} \frac{x^2}{w^2} + \frac{x^3}{w^3} \right), \quad [\text{S5a}]$$

as used in the main text.

To simplify analyzing the accumulation behavior, Eq. S3 is nondimensionalized. Introducing the dimensionless constants $\tau = Dt/w^2$, $q = v_0 w/D$, $p = S_T \Delta T$, $\eta = y/w$, $\xi = x/w$, Eq. S3 is transformed to

$$\frac{\partial c}{\partial \tau} = \left(\frac{\partial^2 c}{\partial \xi^2} + \frac{\partial^2 c}{\partial \eta^2} \right) + p \frac{\partial c}{\partial \xi} + q f(\xi) \frac{\partial c}{\partial \eta} \quad [\text{S6}]$$

with $f(\xi)$ being $f(\xi) = (1/2\xi - 3/2\xi^2 + \xi^3)$.

For the purpose presented in the main text, the steady-state distribution of concentration is of interest; i.e., $\partial c/\partial \tau = 0$. The key to solving Eq. S6 in the steady state is a separation of variables. We choose $c(\xi, \eta) = U(\xi)V(\eta)$ with an exponential dependence in the long η axis $V(\eta) = \exp(\alpha\eta)$, where the factor α is to be

determined. Plugging the ansatz into Eq. S6 yields a differential equation for $U(\xi)$:

$$U'' + pU' + (\alpha^2 + \alpha q f(\xi))U = 0. \quad [\text{S7}]$$

The natural boundary conditions enforce that no flux of particles is crossing the walls of the compartment; hence diffusive and thermodiffusive currents have to cancel at the boundary. In terms of $U(\xi)$ this means $U' + pU = 0$ at $\xi = 0, 1$. Eq. S7 can only simultaneously obey both boundary conditions for a distinct α , hence defining the exponential accumulation. Solving Eq. S7 can be done numerically by standard computational techniques.

In contrast, one can compute an analytic solution in the limit $p \ll 1$, which is presented in the following. We expand U and α to second order in p and get $U = 1 + pU_1 + p^2U_2 + \dots$, and $\alpha = p\alpha_1 + p^2\alpha_2 + \dots$. To get a uniform distribution for $p = 0$, we choose the zeroth order of U arbitrarily to be unity and that of α to be zero. Inserting the expansions into Eq. S7 and collecting orders of p gives

$$p^1 : U_1'' + \alpha_1 q f(\xi) U_1 = 0 \quad [\text{S8a}]$$

$$p^2 : U_2'' + U_1' + \alpha_1^2 + \alpha_2 q f(\xi) + \alpha_1 q f(\xi) U_1 = 0. \quad [\text{S8b}]$$

The second-order differential Eq. S8a can be solved by direct integration, while enforcing the boundary conditions of first order in p , $U_1' + 1 = 0$ at $\xi = 0, 1$. Subsequently, the result is inserted into Eq. S8b, which can once again be solved by direct integration. Enforcing the boundary conditions of second order in p , $U_2' + U_2 = 0$ at $\xi = 0, 1$, fixes the exponent $\alpha \approx p\alpha_1$. For gravitational pumping the exponent is $\alpha \approx 84pq/(10,080 + q^2)$ and the distribution inside the trap (Fig. S2E) is

$$c(\xi, \eta) = \left(1 + p \left(-\xi + \frac{84pq}{10,080 + q^2} \left(\frac{1}{20} \xi^5 - \frac{1}{8} \xi^4 + \frac{1}{12} \xi^3 \right) \right) \right) \times \exp \left(\frac{84pq}{10,080 + q^2} \eta \right). \quad [\text{S9a}]$$

The exponential accumulation is maximal for an optimal $q_{opt} = \sqrt{(10,080)} \approx 100$, where the exponent has its maximum, $\alpha_{max} \approx 0.42p$. Because velocity is coupled to the width of the trap, optimal $q_{opt} = v_0 w/D$ means optimal width.

The choice of width and thus convection speed is crucial for the accumulation behavior. Diffusion decreases with RNA/DNA length, and thus the optimal width decreases as well. If the width is chosen such that monomers are accumulated optimally, then the buildup of longer polymers will decrease the accumulation efficiency. If, on the other hand, the width is chosen to optimally accumulate long polymers, then polymerization escalates inside the trap.

b) Laser-driven trap. A laser can be used to evoke a thermal molecule trap (Fig. 3) analogously to the gravitational thermal molecule trap discussed above. The advantage is that several parameters of the system, such as convection velocity, temperature gradient, and width of the trap, can be modified independently. Also a symmetrical trap can be generated to not depend on the geometry of a hard-to-define trap ending. Solvent flux and temperature gradient are directly evoked by an IR laser moving along the center line of a glass capillary. Due to the expansivity of water, the solvent flows in the opposite direction of the laser movement. At the edges of the linear IR laser pathway the solvent naturally reverses and flows back along the outside edge of the capillary, creating two symmetric convection rolls along the long axis. This setup would accumulate molecules at one corner, where they could easily escape via diffusion. To prevent this from happening the capillary could be either closed physically, like the gravitationally driven thermal molecule

trap, or closed using mirror-inverted pumping along the short axis of the trap. This induces four symmetric convection rolls, each of them trapping analogous to the gravitationally driven trap (Fig. S2A–C). In the following we calculate the accumulation for one these four identical traps. The a velocity pattern is symmetric to the center line of the trap, having the global velocity maximum in the center and velocity maxima of opposite sign close to the edges of the trap. The profile is modeled analogous to Eq. S5a, by assuming that the third spatial derivative of the velocity is constant, $\partial^3 v / \partial x^3 = \text{const}$. The result was qualitatively verified using bead tracking. Furthermore, slip-flow boundaries are enforced; i.e., $v(0) = 0$, $v(w) = v_0$. The choice of coordinates is such that the origin of x is at one cold wall and $x = w$ in the center of the trap. As side conditions we demand the profile to be continuous, i.e., $\partial v / \partial x = 0$ at $x = w$, and a drift-free trap. This yields the velocity profile (Fig. S2D)

$$v(x) = v_0 \left(6 \frac{x}{w} - 15 \frac{x^2}{w^2} + 8 \frac{x^3}{w^3} \right) \quad [\text{S5b}]$$

To simplify the analysis of the accumulation behavior, Eq. S3 is nondimensionalized. Identically to gravitational pumping, the dimensionless constants $\tau = Dt/w^2$, $q = v_0 w / D$, $p = S_T \Delta T$, $\eta = y/w$, $\xi = x/a$ are introduced. The pumping velocity v_0 can be adjusted by laser movement. The velocity profile $f(\xi) = (6\xi - 15\xi^2 + 8\xi^3)$ leads to an accumulation exponent $\alpha \approx 189pq/1,260 + 38q^2$ and the distribution in the side trap (Fig. S2E)

$$c(\xi, \eta) = \left(1 + p \left(-\xi + \frac{189pq}{1,260 + 38q^2} \left(\frac{2}{5}\xi^5 - \frac{3}{4}\xi^4 + \frac{1}{2}\xi^3 \right) \right) \right) \times \exp \left(\frac{189pq}{1,260 + 38q^2} \eta \right). \quad [\text{S9b}]$$

Here, the exponent has its maximum $\alpha_{\max} \approx 0.43p$ at an optimal $q_{\text{opt}} = \sqrt{630/19} \approx 5.8$. A 2D finite-element simulation was used to describe the experimental laser trap, where a laminar fluid drift through the capillary allowed for reasonable experimental time-scales. The assumption that a 2D simulation may describe the 3D experiment is valid in this regard because the prominent driving force of convection and thermophoresis, the varying temperature profile, is y symmetric and has only small deviations along the z axis. The 2D/3D difference of the convection flow is small for the fast thermoviscous pumping used in the experiment as shown in ref. 2. Therefore, the match of the simulation and the 2D projection of the experiment obtained by fluorescence microscopy is reasonable (Figs. 3 and 4).

Quasi-1D Calculation of the Accumulation. In the following, an approximate solution of the accumulation inside the trap for fast chemical reactions is derived. In this limit, the polymerization reaction equilibrates adiabatically to the steady-state solution $c_n = c_1^n \prod k_{\text{tr}}^{\text{on}} / k_{\text{tr}}^{\text{off}}$ during the accumulation of the thermal trap. For this reason we define effective constants of the system, such as the diffusion coefficient

$$\bar{D} = \frac{\sum c_n n D(n)}{\sum c_n n}$$

and Soret coefficients

$$\bar{S}_T = \frac{\sum c_n n S_T(n)}{\sum c_n n},$$

which account for the combined effects of the individual polymers. The diffusion and Soret coefficients for double-stranded (ds)DNA used in the main text and for dsDNA in the experimen-

tal conditions in Figs. 3 and 4 are $D(n) = 65n^{-0.75} \mu\text{m}^2/\text{s}$ and $S_T(n) = 0.1n^{0.5} \text{K}^{-1}$. In the warm and salty scenario for RNA shown in Fig. 2, the experimental scaling laws $D(n) = 643n^{-0.46} \mu\text{m}^2/\text{s}$ and $S_T(n) = (5.3 + 5.7n^{0.73}) \times 10^{-3} \text{K}^{-1}$ were used (5). The largest change in diffusion and Soret coefficients is the exponential accumulation along the long axis of the trap, because this alters the length distribution c_n toward longer molecules. Furthermore the influence of concentration variation along the short axis and the concentration distribution change due to the temperature-dependent dissociation constant are two minor, temperature-dependent contributions. Assuming that the temperature difference ΔT is small, one can neglect both latter contributions. Although assuming a small concentration variation along the short axis is almost always justified, here variations are only of order $p = S_T \Delta T$, and the second assumption may cause inaccuracies due to the exponential impact of temperature differences on the dissociation constant for too large ΔT . Following the simplification, the dependence of diffusion and Soret coefficients, D and S_T , becomes effectively one-dimensional, along the y axis. Thus, the system can be sliced along y into infinitesimal disks of constant D and S_T and solved in an integrative manner:

$$c(x, y) = U(x, c(x, y)) \exp \left(\int_0^y d\tilde{y} \alpha(c(x, \tilde{y})) \right). \quad [\text{S10}]$$

As a top boundary condition we use the solution of Eq. S3 and use c_{out} as concentration. U and α can be obtained either numerically or analytically, as described above.

SI Text B. Experiment

Materials and Methods. We use a custom-made borosilicate capillary (VitroCom) with a rectangular cross section of $100 \times 50 \mu\text{m}$. The capillary is embedded into immersion oil to improve the optical quality of the system and sandwiched between an IR-transparent silicon wafer and a sapphire coverslip to enhance thermal gradients. The silicon wafer is cooled with Peltier elements (9502/065/018M; Ferrotec) at 10°C to ensure constant temperature for long time measurements. The temperatures inside the capillary are set to $T_{\min} = 53^\circ\text{C}$ and $T_{\max} = 60^\circ\text{C}$ over a range of $50 \mu\text{m}$ by IR laser absorption.

The filled capillary is connected to a high-precision syringe pump (neMESYS; Cetoni) on one side for automatic refilling. Imaging is done with a fluorescence microscope (Axiotech Vario; Zeiss), using a set of high-power light-emitting diodes (LEDs) for alternating color excitation (590 nm and 470 nm; Thorlabs) and a $40\times$ objective (Plan-Neofluar $40\times 0.9 \text{NA}$; Zeiss). A CCD camera (Sensicam; PCO) records color-separated fluorescence resonance energy transfer (FRET) images provided by a dual-view unit (Optosplit II; Cairn Research). Because the molecule trap creates DNA concentration differences of several orders of magnitude, each excitation channel (blue, amber) was recorded with three different LED settings (10 mA, 20 mA, and 80 mA) to improve the signal's dynamic range. With dual excitation and dual emission, six CCD frames and 12 images were recorded at each time frame. FRET probability was calibrated as described below.

Heating and thermoviscous flow are provided by an IR laser (TLR-20-1940; IPG Photonics) from the bottom. It is focused inside the capillary with a custom-built scanner lens system providing a constant heat-spot width of $30 \mu\text{m}$ along the whole-scan range of $2 \times 3.5 \text{mm}$. The scanner lens system consists of three lenses (L_A , Linos, G063095000, $f = 15 \text{mm}$; $L_B = L_C$, Thorlabs, LA1422-C, $f = 40 \text{mm}$) with lens separations of $\Delta x_{L_A, L_B} = 57 \text{mm}$, $\Delta x_{L_B, L_C} = 45 \text{mm}$, and $\Delta x_{L_C, \text{scanner}} = 10 \text{mm}$. Angular deflection is realized by scanning mirrors (6200-XY; Cambridge Technology). A heat bath (F12; Julabo) cools the microscopy stage and the scanning mirrors. The thermoviscous fluid flow is created by a di-

rected/asymmetric movement of the IR laser along the capillary: Each time the laser spot passes by, a small amount of water is transported opposite to the direction of the laser spot movement (6).

To realize a reversible and observable polymerization reaction, we designed pieces of double-stranded DNA (95 bp) that define a monomer (Fig. 3A) with two complementary sticky ends of 25 bases (IBA Lifesciences). The sequences of the monomer are

DNA_A : 3' TGTGAGACCCCCGGTCACTGATGAGGAGG-AGCTGCGGACTCCCGTGAACCAGAACTCTCGGGGAAT-CCATCAACTTGGCCGGTAAGGGGTCGCGAATAACG-TG(ROX)ACGTACATCGGGACT 5'

DNA_B : 5' GTTATTGCAG(FAM)TGCATGTAGCCCTGAA-CACTTGGGGCCAGTGACTACTCCTCGACGCCT-GAGGCACCTGGTCTTGAGAGCCCCTTAGGTAGTTGA-ACCGCCATTCCCCAGGGC 3'.

DNA arrived as an aqueous solution with a concentration of 100 μ M and was portioned into aliquots of 50 μ L and frozen immediately. The final concentrations of the working stock are 10 μ M of DNA_A and DNA_B , respectively, inside a 1 \times PBS buffer (137 mM NaCl, 2.7 mM KCl, 10 mM $Na_2HPO_4 \cdot H_2O$, 2 mM KH_2PO_4). The stock solution was annealed into a defined state before further dilution, using a temperature ramp from 95 $^{\circ}C$ to 10 $^{\circ}C$ with a cooling rate of 1 $^{\circ}C/10$ s.

Each sticky end was modified with the fluorescent dye carboxy-X-rhodamin (ROX) or its respective FRET counterpart fluorescein amidite (FAM). The polymerization of two monomers at their complementary sticky ends brings both dyes in close proximity and is recorded by fluorescence resonance energy transfer.

Because we used FRET in a bulk solution at various temperatures, prior calibration had to be done. We recorded the temperature dependence of the spatially averaged FRET signal obtained by

$$FRET(T) \equiv \frac{DA(T) - dd(T) * DD(t) - aa(T) * AA(T)}{AA(T)}, \quad [S11]$$

where the channels are defined according to Tables S1 and S2.

The temperature-dependent crosstalk corrections $dd(T)$ and $aa(T)$ were recorded over a temperature range of 10–95 $^{\circ}C$, using the same monomers with nonsticky ends to prevent binding artifacts in the fluorescence signal. For measurements of $dd(T)$ ($aa(T)$), the monomers were labeled with 6-FAM (6-ROX) only. After obtaining coefficients $\alpha \equiv \min(FRET(T))$ and $\beta \equiv \max(FRET(T)) - \alpha$ by Eq. S11, the normalized, crosstalk-corrected, and time-dependent FRET ratio for each pixel (x,y) and frame t is defined as

$$FRET(t,x,y) \equiv \left(\frac{DA(t,x,y) - dd(T(x,y)) * DD(t,x,y) - aa(T(x,y)) * AA(t,x,y) - \alpha}{AA(t,x,y)} \right) / \beta, \quad [S12]$$

where $T(x,y)$ is the previously measured temperature profile inside the trap. This procedure was repeated for each illumination setting.

To determine the 2D temperature profile $T(x,y)$ inside the filled capillary, we switched off the thermoviscous fluid flow but left the temperature profile of the molecule trap unchanged before each trapping measurement: Superposition of the initial movement with a reversed movement of the IR laser spot results in a vanishing net flow inside the capillary while IR absorption is kept constant. We compared the steady-state FRET signal under these conditions with the temperature-dependent FRET calibration measurement done before using thermoelectric elements. Fluid flow velocity was recorded by tracking homogeneously distributed

1- μ m green fluorescent silica particles (PSI-G1.0NH2; Kisker), using the same experimental settings as in the polymerization trap. The mean fluid speed was determined to be 28 ± 2 μ m/s. The silica beads used in this measurement exhibit a considerably lower diffusion coefficient compared with DNA (5). Accordingly the beads are not trapped but continuously cycled between the hot and the cold sides of the compartment. Clay (7) with similar slow diffusion could therefore act as a catalyst for nucleotide-based reactions on the cold side, while their surface is being reset for another cycle at the hot side.

The only fitting parameter of the polymer theory, the dissociation constant $K_{D,polymer}$ of the monomer's hybridization bond, was checked independently with thermal melting-curve analysis (Fig. S3A) and calculated with $K_{D,melting} = FRET(T) / (2 \cdot c_0 (1 - FRET(T))^2)$ for a solution of 2 μ M monomers buffered in 1 \times PBS (8). The dissociation constants revealed by both methods match within the error margin. The chosen temperature of $T = 56$ $^{\circ}C$ is the temperature at the point of measurement in the polymerization experiment (Fig. S3A). The measured, temperature-dependent dissociation constant was also taken into account for the finite-element simulation and mapped over the temperature profile. The free energy of the hybridization bond is estimated with a linear fit of the dissociation constant over the inverse absolute temperature with $\Delta G^0 / R \cdot 1/T + \text{const.} = \ln(K_D)$. The obtained value of 45 kcal/mol matches the modeled value of 48 kcal/mol for the bond energy (determined using IDT OligoAnalyzer). An approximation for the relative change of K_D over temperature is

$$\frac{dK_D/dT}{K_D} = \frac{\Delta G^0}{R \cdot T^2}. \quad [S13]$$

Whereas the temperature-dependent and measured K_D was used in the finite-element simulation, K_D was assumed to be temperature averaged in the theoretical considerations. Eq. S13 justifies this assumption for theoretical calculations concerning the experimental model system, because K_D varies less than one order of magnitude within the given temperature range. In the case of RNA polymerization, the theoretical results represent a lower bound for the escalated polymerization, because the affinity of polymerization is higher in colder regions of the trap, especially in the trapping center at the bottom edge.

The complexity of the experimental system does not allow a full analytical description, but is accessible with a combination of an analytical polymerization solution and a finite-element simulation

of the thermal trap. Therefore, we combined the semianalytical polymerization theory with a 2D hydrodynamic finite-element simulation. Because the characteristic timescale of polymerization is much shorter compared with trapping dynamics, we may correlate all DNA length-dependent parameters (thermodiffusion/diffusion coefficients) of the system to the total concentration of monomers at a specific time and place, using $\bar{D}(c_0)$ and $\bar{S}_T(c_0)$ (main text). Convective and drift flow velocity, temperature-dependent K_D , and temperature profile were set to experimental values (Fig. 3C). The simulated capillary geometry includes a passive area without heating or thermoviscous pumping at the outer boundaries of the trap to fully model the experimental setup. The positions used for extracting experimental and

simulation data are the trapping center itself (center) and a relative distance of 4.9 mm from the trapping center (edge). Fig. S3B clarifies the two steady states of the accumulation ratio $\sum kC_{k,center} / \sum kC_{k,edge}$ and the absolute monomer concentration $\sum kC_{k,center}$ by showing the time evolution of the total amount of monomers integrated over the simulated trapping area.

SI Text C. Primordial Scenario

The model presented in the main text can in principle be extrapolated to any arbitrary primordial scenario, concerning temperature, salt concentration, or geological geometries. Here we discuss two additional plausible scenarios, a cold and saline scenario (e.g., an arctic ocean) and a salt-deprived scenario (e.g., a primordial freshwater pond). For this purpose we measured the parameters of the system, i.e., diffusion D and Soret coefficient S_T for different salt concentrations, DNA or RNA lengths, and temperatures as shown in Fig. S3 C and D for the two settings.

Whereas the former scenario is comparable to modern biological environments, the latter has been proposed by Szostak and colleagues as these conditions could facilitate development

of protocells out of simple fatty acids (9) and could therefore be a link from early molecular evolution to the first compartmentalization of life on earth. The cold and salty ocean was modeled assuming 25 °C (which is cold compared with the typical 60 °C of primordial oceans) and a salt concentration of 150 mM NaCl ($\lambda_{Debye} = 0.8$ nm). The lower concentration slightly decreases the effect of thermophoresis, but can easily be compensated by a slightly longer trap length.

In freshwater, in contrast, the low salt concentrations enhance the effect of thermophoresis significantly and the hyperexponential escalation sets in at even shorter trap heights, as shown in Fig. S4, II. Here the temperature is assumed to be at 55 °C and salt concentration at 3 mM NaCl ($\lambda_{Debye} = 5.6$ nm). We restricted ourselves to investigating only geological boundary conditions, but not the chemical means of polymerization because our fully reversible polymerization model represents the most inefficient polymerization reaction and therefore gives a lower bound for polymer lengths. Stable covalent bonds, for example, are often modeled using irreversible polymerization, which would quickly lead to incorporation of all building blocks into very long polymers.

1. Baaske P, et al. (2007) Extreme accumulation of nucleotides in simulated hydrothermal pore systems. *Proc Natl Acad Sci USA* 104(22):9346–9351.
2. Mast CB, Braun D (2010) Thermal trap for DNA replication. *Phys Rev Lett* 104(18):188102.
3. Miller ES, et al. (2003) Bacteriophage T4 genome. *Microbiol Mol Biol Rev* 67(1):86–156.
4. Rosenbloom J, Cox EC (1966) Sedimentation coefficient of T-even bacteriophage DNA. *Biopolymers* 4(7):747–757.
5. Dühr S, Braun D (2006) Why molecules move along a temperature gradient. *Proc Natl Acad Sci USA* 103(52):19678–19682.
6. Weinert FM, Braun D (2008) Optically driven fluid flow along arbitrary microscale patterns using thermoviscous expansion. *J Appl Phys* 104:104701-1–104701-10.
7. Ferris JP, Hill AR, Jr., Liu R, Orgel LE (1996) Synthesis of long prebiotic oligomers on mineral surfaces. *Nature* 381(6577):59–61.
8. Mergny J-L, Lacroix L (2003) Analysis of thermal melting curves. *Oligonucleotides* 13(6):515–537.
9. Ricardo A, Szostak JW (2009) Origin of life on earth. *Sci Am* 301(3):54–61.

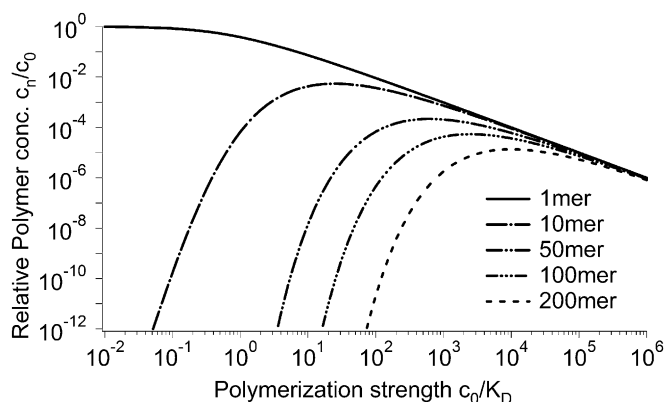


Fig. S1. Equilibrium distribution of polynucleotide lengths. Hydrolysis constantly cleaves polynucleotides, leading to finite lengths of polynucleotides in equilibrium. For total monomer concentrations $c_0 = \sum n c_n$ lower than the dissociation constant, virtually only monomers are present. For concentrations larger than the dissociation constant, a large share of polynucleotides is built up. 200-mers abruptly appear for $c_0/K_D > 10^2$.

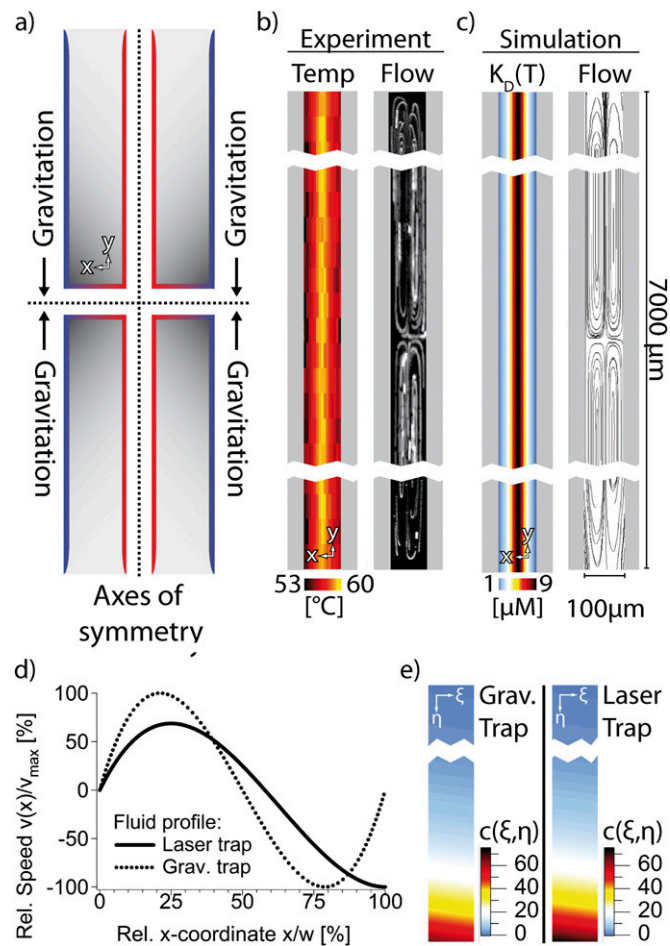


Fig. S2. Connection of theory, simulation, and experiment. (A) A gravitational trap is driven by a thermal gradient and the buoyancy of water. Therefore, it has a fixed relation between the diffusion coefficient of the species to be accumulated and the optimal width of the trap. In a laser-driven trap, the convection speed can be set independently of the temperature gradient, which allows having an optimal convection speed for any species of biomolecules in a given trap width. The geometry of the laser-driven trap can be thought of as four gravitational traps glued together at their hot and bottom sides with symmetric boundary conditions. (B) The 2D temperature and profile were measured using the temperature-dependent dye 2',7'-bis-(2-carboxyethyl)-5-(and-6)-carboxyfluorescein and tracking fluorescent beads. (C) A 2D finite-element simulation simulates the experiment. We used the theoretical concentration-dependent diffusion coefficient $D(c)$ and Soret coefficient $S_T(c)$ to take into account the timescale-separated polymerization reaction. The temperature-dependent dissociation constant $K_D(T)$ was measured separately (Fig. S3) and was mapped to the temperature profile inside the trap. Therefore, all relevant experimental parameters [$K_D(T)$, temperature, convection flow, degree of polymerization, and monomer concentration] could be successfully modeled (Fig. 4). (D) Convection flow $v(x)$ according to Eq. S5a (gravitation trap: dashed line) and Eq. S5b (laser trap: solid line). The difference comes from the missing nonslip boundary in the center of the capillary; however, it has no significant effect on the trapping efficiency. (E) Concentration distribution $c(\xi, \eta)$ according to Eq. S9a (gravitation trap) and Eq. S9b (laser trap) for RNA nucleotides with $S_T = 0.01 \cdot 1/K$, $\Delta T = 10$ K, $p = S_T \cdot \Delta T = 0.1$, $q_{grav,opt} = 100$ for the gravitation trap, $q_{laser,opt} = 5.8$ (SI Text A and B) for the laser trap, and an exemplary trap aspect ratio of 1:100.

